Physicochemical and Electrochemical Properties of $K[N(SO_2F)_2]$–[*N*-Methyl-*N*-propylpyrrolidinium][$N(SO_2F)_2$] Ionic Liquids for Potassium-Ion Batteries

Takayuki Yamamoto,[*,†] Kazuhiko Matsumoto,[‡,§] Rika Hagiwara,[‡,§] and Toshiyuki Nohira[*,†,§]

†Institute of Advanced Energy, Kyoto University, Uji 611-0011, Japan

‡Graduate School of Energy Science, Kyoto University, Sakyo-ku, Kyoto 606-8501, Japan

§Unit of Elements Strategy Initiative for Catalysts & Batteries (ESICB), Kyoto University, Katsura, Kyoto 615-8510, Japan

ABSTRACT

The physicochemical and electrochemical properties of the binary ionic liquid, K[FSA]–[C_3C_1pyrr][FSA] (FSA = bis(fluorosulfonyl)amide; C_3C_1pyrr = *N*-Methyl-*N*-propylpyrrolidinium), were investigated at 253–393 K, with the aim of developing a new electrolyte for potassium-ion batteries (K-ion batteries; KIBs). A phase diagram was constructed from the results of differential scanning calorimetry measurements and revealed that the melting point of this ionic liquid is below room temperature for compositions of x(K[FSA]) = 0–0.25

(*x*(K[FSA]) = molar fraction of K[FSA]). The viscosity, ionic conductivity, and density were measured for *x*(K[FSA]) = 0–0.25. The ionic conductivity when *x*(K[FSA]) = 0.20 was 4.8 mS cm^{-1} at 298 K, which is higher than that for the equivalent sodium and lithium ionic liquids. Cyclic voltammetry measurements of M[FSA]–[C_3C_1pyrr][FSA] ionic liquids (*x*(M[FSA]) = 0.20; M = K, Na, or Li) indicated that potassium metal deposition/dissolution occurs at a more negative potential than that for lithium and sodium deposition/dissolution, suggesting that KIBs with a high operating voltage can be constructed using K[FSA]–[C_3C_1pyrr][FSA] as an ionic liquid electrolyte.

1. INTRODUCTION

Establishing a low-carbon society is one of our big challenges in addressing environmental problems and energy issues. Combining renewable energy resources and large-scaled electrical energy storage (EES) devices is considered to be the most desirable and feasible solution. Lithium-ion batteries (Li-ion batteries; LIBs) are good candidates for EES devices because of their high energy density.[1,2] Although LIBs are already applied in portable electronic devices such as mobile phones and PC laptops, there are two main concerns regarding the extension to large-scaled LIBs. One is the utilization of limited and unevenly distributed resources of lithium and cobalt for the electrode and/or electrolytes, which may lead to supply instability and price increases in the future.[3,4] The other is the potential risk of ignition accidents due to the flammable and volatile organic solvent-based electrolytes used in current LIBs; this is a particular concern for large-scaled devices such as stationary batteries and electric vehicles.

Several research groups, including our own, have focused on sodium-ion batteries (Na-ion batteries; NIBs) using ionic liquid electrolytes to solve the aforementioned problems.[5–16] Sodium

resources are abundant in the earth's crust and in seawater, and ionic liquids are nonflammable and negligibly volatile, which enables the construction of low-cost and safe batteries. However, since the standard redox potential of sodium is higher than that of lithium, the operating voltage of NIBs is inherently lower than that of LIBs when using the same framework for the positive electrodes, which remains as a drawback of NIBs. Thus, there is a strong demand to develop a new battery that combines low cost and high performance. In the present study, we focused on potassium-ion batteries (K-ion batteries; KIBs) as next-generation energy storage devices. Potassium resources are much more abundant compared with lithium resources, and comparable to sodium resources.[17] The standard redox potential of K^+/K is more negative than that of Na^+/Na. Moreover, in a certain type of organic solvent[18,19] and molten salt (ionic liquid)[20–22], the redox potential of K^+/K is more negative than that of Li^+/Li, implying that the operating voltage of KIBs is higher than that of LIBs. Furthermore, the K^+ ion is a weaker Lewis acid than Li^+ and Na^+ ions, which gives KIBs two main advantages over LIBs and NIBs: faster ion transport in the bulk KIB electrolytes due to the smaller Stokes radius of solvated K^+ ions,[19] and faster electrode reactions due to the lower desolvation energy of K^+ ions.[23] In addition, inexpensive aluminum current collectors can be used for the negative electrode of KIBs, since aluminum does not form intermetallic compounds with potassium,[24] which is not the case in LIBs.

Despite the many benefits of KIBs, no intense studies were conducted until very recently.[25,26] In the early studies, the electrochemical behavior of Prussian blue-based compounds has been investigated in aqueous electrolytes,[27–31] and these materials have also been found to work as positive electrodes of KIBs using organic-solvent-based electrolytes.[32–34] Recently, several inorganic compounds, including layered oxides,[35–37] phosphates,[38–41] and sulfates,[42] were found to be active positive electrode materials. Reports on negative electrodes for KIBs are mainly

categorized into carbonaceous materials (graphite,[19,34,43–46] hard carbon,[47] and soft carbon[36]), alloy compounds (Sn,[48] Sn_4P_3,[49] and Sb[50]), and titanium-based compounds.[51,52] However, all of these studies utilized organic solvent-based electrolytes. There are few reports on KIBs using safer ionic liquid electrolytes.[53]

Based on these studies, we focused on K[FSA]–[C_3C_1pyrr][FSA] ionic liquid (FSA = bis(fluorosulfonyl)amide; C_3C_1pyrr = *N*-methyl-*N*-propylpyrrolidinium) as a new KIB electrolyte. [C_3C_1pyrr][FSA] ionic liquid has been well studied as an electrolyte for NIBs[7,9,14,15] and LIBs[54–57], because of its reasonably high ionic conductivity and superior electrochemical stability at room temperature. In the present study, the physicochemical and electrochemical properties of K[FSA]–[C_3C_1pyrr][FSA] ionic liquid were investigated. The phase transition temperatures were determined by differential scanning calorimetry (DSC) and used to construct a phase diagram. Its viscosity, ionic conductivity, and density were measured over a wide temperature range between 258 and 393 K. The composition of x(K[FSA]) = 0.20 (x(K[FSA]) = molar fraction of K[FSA]) was selected for electrochemical measurements, and its electrochemical window was determined using cyclic voltammetry. Finally, the obtained results were compared with sodium and lithium counterparts, and the feasibility of high-voltage KIBs was discussed.

2. EXPERIMENTAL SECTION

K[FSA] (> 99+%; Mitsubishi Materials Electronic Chemicals Co., Ltd.), Na[FSA] (> 99+%; Mitsubishi Materials Electronic Chemicals Co., Ltd.), Li[FSA] (> 99+%; Kishida Chemicals Co., Ltd.), and [C_3C_1pyrr][FSA] (> 99.9%; Kanto Chemical Co., Inc.) were dried under vacuum at 353 or 333 K for 48 h prior to use. K[FSA]–[C_3C_1pyrr][FSA] ionic liquids with various

compositions (x(K[FSA]) = 0.05, 0.10, 0.15, 0.20, 0.25, 0.30, 0.40, 0.50, 0.60, 0.70, 0.80, and 0.90; x(K[FSA]) = molar fraction of K[FSA]) were prepared by mixing K[FSA] and [C_3C_1pyrr][FSA] in an argon-filled glove box. All ionic liquids were handled under a dry argon atmosphere. Phase transition temperatures, such as the melting point, of this ionic liquid were measured using differential scanning calorimeter (DSC; Thermo plus EVO2 DSC8230L, Rigaku Co.). Ionic conductivity values were determined from AC impedance measurements using a T-shaped cell made of polytetrafluoroethylene (PTFE) and a chemical impedance analyzer (3532-80, Hioki E. E. Corp.). The cell constant was determined using a 0.1 M KCl aqueous solution. Viscosities and densities were measured using an electromagnetically spinning viscometer (EMS-1000, Kyoto Electronics Manufacturing Co., Ltd.) and a vibration-type density meter (DMA 4500 M, Anton Paar, Ltd.), respectively.

Cyclic voltammetry was conducted using electrochemical measurement apparatus (HZ-7000, Hokuto Denko Corp.) and a three-electrode beaker cell. A copper disk (negative potential region) and a glassy carbon disk (positive potential region) were used as working electrodes. These electrodes were polished by alumina abrasives dispersed in water and then dried before measurement. Platinum mesh was used as the counter electrode. A silver wire immersed in [C_3C_1pyrr][FSA] ionic liquid containing 50 mmol dm^{-3} silver trifluoromethanesulfonate ($AgCF_3SO_3$) was used as the reference electrode. The reference electrode compartment was separated from the main cell by a porous Vycor glass filter. M[FSA]–[C_3C_1pyrr][FSA] ionic liquids (x(M[FSA]) = 0.20; M = K, Na, and Li) were used as the electrolyte for these measurements. The obtained cyclic voltammograms were calibrated to the potential of the ferrocenium/ferrocene redox couple (Fc^+/Fc), which was measured after adding 10 mmol dm^{-3}

ferrocene to the electrolyte. The scan rate and measurement temperature were 5 mV s^{-1} and 298 K, respectively.

3. RESULTS AND DISCUSSION

3.1. Physicochemical properties

Figure 1 shows the phase diagram for K[FSA]–[C_3C_1pyrr][FSA] ionic liquid, and **Table 1** summarizes its phase transition temperatures based on DSC curves (**Figures S1–S14**). The melting points of the single K[FSA] and [C_3C_1pyrr][FSA] salts are 380 and 269 K, respectively, consistent with previous reports.[12,15] The single [C_3C_1pyrr][FSA] salt also shows two endothermic peaks below its melting point at 191 and 253 K, which correspond to the solid-solid phase transition. In the composition region of x(K[FSA]) = 0–0.25, the melting points decreases with increasing x(K[FSA]). However, the melting point suddenly increase to 355 K at x(K[FSA]) = 0.30, indicating that the eutectic point lies between x(K[FSA]) = 0.25 and 0.30. In fact, a small amount of precipitate was found in the x(K[FSA]) = 0.30 melt at room temperature. For compositions of x(K[FSA]) > 0.30, the melting point increases with increasing x(K[FSA]). Some compositions (x(K[FSA]) = 0.60–0.90) show endothermic peaks at around 190 and 240 K, corresponding to the solid-solid phase transition of [C_3C_1pyrr][FSA] and the eutectic point, respectively. Consequently, it is reasonable to conclude that there are no intermediate compounds in this system. In addition, supercooling and glass transition behavior are observed in the compositional range of x(K[FSA]) = 0.20–0.70. From a viewpoint of battery application, ionic liquids with melting points lower than room temperature are desirable; thus, we measured various physicochemical properties of K[FSA]–[C_3C_1pyrr][FSA] within a compositional range of x(K[FSA]) = 0–0.25.

An Arrhenius plot of viscosity is presented in **Figure 2**. Lower viscosity values are observed at higher temperatures and lower x(K[FSA]) values. For all compositions, the Arrhenius plots cannot be fitted by straight lines. The deviation from the Arrhenius plots is often corrected by the VTF (Vogel–Tammann–Fulcher) equation (**Equation 1**).[58]

$$\eta(T) = A_\eta T^{1/2} \exp\left(\frac{B_\eta}{T - T_{0\eta}}\right) \quad (1)$$

where $\eta(T)$ is the viscosity, A_η is a constant related to the viscosity at infinite temperature, B_η is a constant related to the activation energy, and $T_{0\eta}$ is the ideal glass transition temperature, which is usually lower than the glass transition temperature (T_g) as determined by DSC measurements. The viscosity values and VTF parameters are summarized in **Tables 2** and **S1**, respectively. In comparison with our previous study,[15] the K[FSA]–[C_3C_1pyrr][FSA] ionic liquids show lower viscosities than their sodium counterparts, indicating that potassium salt possesses a higher fluidity than sodium salt.

Figure 3 shows Arrhenius plots for the ionic conductivity. The ionic conductivity increases with increasing temperature and decreasing x(K[FSA]). The x(K[FSA]) = 0.20 melt exhibits an ionic conductivity of 4.8 mS cm^{-1} at 298 K (**Table 3**). This value is higher than those for the sodium (3.6 mS cm^{-1})[15] and lithium (ca. 3.6 mS cm^{-1})[56] counterparts at the same x(M[FSA]) value and temperature. This is because K^+ ions possess lower Lewis acidity, resulting in superior ionic mobility in potassium-based ionic liquids. This tendency has also been reported in organic solvent-based electrolytes.[19] As in the case of viscosity, the ionic conductivity plots are fitted by the VTF equation (**Equation 2**) (see **Table S2** for VTF parameters):

$$\sigma(T) = A_\sigma T^{-1/2} \exp\left(-\frac{B_\sigma}{T - T_{0\sigma}}\right) \quad (2)$$

where $\sigma(T)$ is the ionic conductivity, A_σ is a constant related to the ionic conductivity at infinite temperature, B_σ is a constant related to the activation energy, and $T_{0\sigma}$ is the ideal glass transition temperature.

Figure 4 and **Table 4** summarize the results of density measurements. The following straight-line equation (**Equation 3**) was used to fit the density plots:

$$\rho(T) = A_\rho T + B_\rho \quad (3)$$

where A_ρ and B_ρ are constants. Molar K^+ ion concentrations calculated from the density values are presented in **Table 5**. At a molar ratio of x(K[FSA]) = 0.20, the K^+ ion concentration is approximately 1 mol dm^{-3} at 298 K, which is almost the same as that for sodium in Na[FSA]–[C_3C_1pyrr][FSA] ionic liquid.[15]

Walden plots showing the relationship between the molar conductivity and inverse viscosity of the K[FSA]–[C_3C_1pyrr][FSA] system are presented in **Figure 5**. These plots lie slightly below the ideal KCl line (denoted as a dotted line), suggesting that this ionic liquid is categorized as a "good" ionic liquid.[59] Moreover, the plots for each composition are straight lines, thus obeying the fractional Walden's rule (**Equation 4**):[59–61]

$$\lambda \eta^\alpha = \text{const.} \quad (4)$$

where λ is the molar conductivity (S cm^2 mol^{-1}) and α is a constant ($0 < \alpha < 1$) corresponding to the slope of the Walden plots. In the present system, the α value is around 0.91–0.92 for compositions of x(K[FSA]) = 0–0.25 (**Table 6**), which is typical for ionic liquids.[15,56,62,63] Assuming that the ideal glass transition temperatures for viscosity and ionic conductivity are almost the same ($T_{0\eta} = T_{0\sigma} = T_0$), the Walden rule can be transformed using **Equations 1** and **2**, as follows (**Equation 5**):

$$\lambda\eta^{\alpha} = \sigma(T)\frac{M}{\rho(T)}\eta(T)^{\alpha} = \frac{A_{\eta}{}^{\alpha}A_{\sigma}T^{(\alpha-1)/2}}{\rho(T)}M\exp\left(\frac{\alpha B_{\eta} - B_{\sigma}}{T - T_0}\right) \quad (5)$$

where M is the formula weight of ionic liquid. Moreover, $T^{(\alpha-1)/2}$ and $\rho(T)$ can be regarded as constants in the limited temperature range according to the results of the Walden plots and the density measurements. Thus, combined with **Equation 4**, the following relationship is obtained (**Equation 6**):

$$\alpha = \frac{B_{\sigma}}{B_{\eta}} \quad (6)$$

The parameter α reflects the ratio of the activation energy for ionic conductivity to that for viscosity. Since the values of T_{η} and T_{σ} are close to each other (**Tables S1** and **S2**), **Equation 6** is applicable for the K[FSA]–[C_3C_1pyrr][FSA] ionic liquid. In addition, according to the VTF fitting results (**Tables S1** and **S2**), the B_{σ}/B_{η} ratios for compositions of x(K[FSA]) = 0–0.25 were calculated to be within a range of approximately 0.87–0.91, which is close to the α values determined from the Walden plot, indicating that the VTF fitting in the present study is reliable.

3.2. Electrochemical properties

Figure 6 shows cyclic voltammograms in M[FSA]–[C_3C_1pyrr][FSA] (M = K, Na, or Li) electrolyte, where x(M[FSA]) = 0.20 (corresponding to ca. 1 mol dm^{-3}), for the 1st cycle at 298 K. The potentials of cyclic voltammograms were calibrated to the Fc^+/Fc redox couple using the data presented in **Figures S15**–**S17**. For all systems, copper and glassy carbon disk electrodes were used to separately investigate the negative and positive potential regions, respectively. As shown in **Figure 6a**, in the negative potential region for the K-ion system, a pair of redox peaks are observed at around –3.3 V vs. Fc^+/Fc. This current behavior is typical of metal deposition and dissolution; as K^+ ions are the only constituent metal ion in this ionic liquid, these redox

currents are attributed to the deposition and dissolution of potassium metal. After reversing the sweep direction from negative to positive, the current changes linearly from a negative value to a positive value. Here, the K^+/K redox potential is determined to be –3.31 V vs. Fc^+/Fc, which is the zero-current potential on the linear current change. This K^+/K redox potential is regarded as the cathode limit potential for the K[FSA]–[C_3C_1pyrr][FSA] ionic liquid. In the positive potential region, an anodic current is observed from ca. 2.4 V vs. Fc^+/Fc during the positive potential sweep. Since almost no corresponding cathodic current appears, this irreversible anodic reaction is assigned to the decomposition of FSA anions, as reported for other FSA-based electrolytes.[13,14,16] In the present study, the anode limit is defined as the potential at which the anodic current reaches 0.1 mA cm^{-2}. According to this definition, the anode limit is 2.41 V vs. Fc^+/Fc for the K[FSA]–[C_3C_1pyrr][FSA] ionic liquid. The electrochemical window is then determined to be 5.72 V. As seen in **Figures 6b** and **6c**, the redox couples derived from alkali metal deposition/dissolution in the negative potential region, and the irreversible anodic current in the positive potential region, are also observed in the equivalent Na-ion and Li-ion systems. The Coulombic efficiencies of alkali metal deposition/dissolution reactions in the 1st cycle are 72.7%, 19.7%, and 84.4% for the K-ion, Na-ion, and Li-ion systems, respectively. The reversibility of potassium metal deposition/dissolution is much better than that of sodium metal, and is even comparable to that of lithium metal, which suggests that the K[FSA]–[C_3C_1pyrr][FSA] electrolyte possesses high reductive stability.

Table 7 summarizes the cathode and anode limit potentials, and the resulting electrochemical windows of the three systems. The K^+/K redox potential is more negative than that of Na^+/Na by 0.35 V and more negative than that of Li^+/Li by 0.24 V. In contrast, the anode limits lie within a narrow potential region of 2.41–2.46 V vs. Fc^+/Fc, indicating that the alkali metal species

scarcely affects the oxidative stability of the FSA anion. Consequently, K[FSA]–[C_3C_1pyrr][FSA] possesses a wider electrochemical window (5.72 V) than those of its Na-ion (5.42 V) and Li-ion (5.48 V) counterparts. Thus, when using FSA-based ionic liquids electrolytes, we envisage that KIBs will work at a higher operating voltage than NIBs and LIBs.

Table 8 compares the differences between the standard potentials of K^+/K and those of Li^+/Li and Na^+/Na in several electrolytes typically used in battery applications, including water and various organic solvents.[18] The K^+/K standard potential is more negative than that of Na^+/Na in all of these electrolytes. In several electrolytes, such as M[FSA]–[C_3C_1pyrr][FSA], propylene carbonate (PC), and acetonitrile (MeCN), the K^+/K redox potential is also more negative than that of Li^+/Li. In particular, the potential difference ($\Delta E^\circ = E^\circ(K^+/K) - E^\circ(Li^+/Li) = -0.24$ V) for the K[FSA]–[C_3C_1pyrr][FSA] ionic liquid is noticeably more negative than that for other electrolytes. These results indicate that KIBs utilizing a K[FSA]–[C_3C_1pyrr][FSA] ionic liquid electrolyte are promising as high-voltage batteries.

4. CONCLUSIONS

In the present study, we have developed a new K[FSA]–[C_3C_1pyrr][FSA] ionic liquid electrolyte for potassium-ion batteries, and evaluated its physicochemical and electrochemical properties. This ionic liquid exhibited a lower viscosity and higher ionic conductivity than its sodium counterpart due to the lower Lewis acidity of potassium ions. For example, the ionic conductivity at a composition of x(K[FSA]) = 0.20 was 4.8 mS cm^{-1} at 298 K, which is high enough to be applied as a battery electrolyte. Cyclic voltammetry measurements using M[FSA]–[C_3C_1pyrr][FSA] (M = K, Na, or Li) showed that the redox potential for potassium metal deposition/dissolution was more negative than those for sodium and lithium

deposition/dissolution, resulting in a wider electrochemical window (5.72 V under the present conditions) for the K^+ ion electrolyte. In conclusion, the K[FSA]–[C_3C_1pyrr][FSA] ionic liquid is promising as a new electrolyte for next-generation K-ion batteries.

■ ASSOCIATED CONTENT

Supporting Information

VTF parameters, DSC curves, cyclic voltammograms of ferrocene (PDF)

■ AUTHOR INFORMATION

Corresponding Authors

*E-mail: yamamoto.takayuki.2w@kyoto-u.ac.jp, Tel: +81-774-38-3498, Fax: +81-774-38-3499 (T.Y.).

*E-mail: nohira.toshiyuki.8r@kyoto-u.ac.jp, Tel: +81-774-38-3500, Fax: +81-774-38-3499 (T.N.).

Notes

The authors declare no competing financial interest

■ ACKNOWLEDGMENTS

Part of this work was performed under management of “Elements Strategy Initiative for Catalysts & Batteries (ESICB)” supported by Ministry of Education, Culture, Sports, Science, and Technology, Japan (MEXT).

■ REFERENCES

(1) Tarascon, J. M.; Armand, M. Issues and Challenges Facing Rechargeable Lithium Batteries. *Nature* **2001**, *414*, 359–367.

(2) Braun, P. V.; Cho, J.; Pikul, J. H.; King, W. P.; Zhang, H. High Power Rechargeable Batteries. *Curr. Opin. Solid State Mat. Sci.* **2012**, *16*, 186–198.

(3) Yabuuchi, N.; Kubota, K.; Dahbi, M.; Komaba, S. Research Development on Sodium-Ion Batteries. *Chem. Rev.* **2014**, *114*, 11636–11682.

(4) Larcher, D.; Tarascon, J. M. Towards Greener and More Sustainable Batteries for Electrical Energy Storage. *Nat. Chem.* **2015**, *7*, 19–29.

(5) Noor, S. A. M.; Howlett, P.C.; MacFarlane, D. R.; Forsyth, M. Properties of Sodium-Based Ionic Liquid Electrolytes for Sodium Secondary Battery Applications. *Electrochim. Acta* **2013**, *114*, 766–771.

(6) Monti, D.; Jónsson, E.; Palacín, M. R.; Johansson, P. Ionic Liquid Based Electrolytes for Sodium-Ion Batteries: Na^+ Solvation and Ionic Conductivity. *J. Power Sources* **2014**, *245*, 630–636.

(7) Yoon, H.; Zhu, H.; Hervault, A.; Armand, M.; MacFarlane, D. R.; Forsyth, M. Physicochemical Properties of *N*-propyl-*N*-methylpyrrolidinium Bis(fluorosulfonyl)imide for Sodium Metal Battery Applications. *Phys. Chem. Chem. Phys.* **2014**, *16*, 12350–12355.

(8) Chagas, L. G.; Buchholz, D.; Wu, L.; Vortmann, B.; Passerini, S. Unexpected Performance of Layered Sodium-Ion Cathode Material in Ionic Liquid-Based Electrolyte. *J. Power Sources* **2014**, *247*, 377–383.

(9) Forsyth, M.; Yoon, H.; Chen, F.; Zhu, H.; MacFarlane, D. R.; Armand, M.; Howlett, P. C. Novel Na^+ Ion Diffusion Mechanism in Mixed Organic–Inorganic Ionic Liquid Electrolyte

Leading to High Na^+ Transference Number and Stable, High Rate Electrochemical Cycling of Sodium Cells. *J. Phys. Chem. C* **2016**, *120*, 4276–4286.

(10) Carstens, T.; Lahiri, A.; Borisenko, N.; Endres, F. [Py1,4]FSI-NaFSI-Based Ionic Liquid Electrolyte for Sodium Batteries: Na^+ Solvation and Interfacial Nanostructure on Au(111). *J. Phys. Chem. C* **2016**, *120*, 14736–14741.

(11) Hasa, I.; Passerini, S.; Hassoun, J. Characteristics of an Ionic Liquid Electrolyte for Sodium-Ion Batteries. *J. Power Sources* **2016**, *303*, 203–207.

(12) Kubota, K.; Nohira, T.; Hagiwara, R. Thermal Properties of Alkali Bis(fluorosulfonyl)amides and Their Binary Mixtures. *J. Chem. Eng. Data* **2010**, *55*, 3142–3146.

(13) Fukunaga, A.; Nohira, T.; Kozawa, Y.; Hagiwara, R.; Sakai, S.; Nitta, K.; Inazawa, S. Intermediate Temperature Ionic Liquid NaFSA–KFSA and Its Application to Sodium Secondary Batteries. *J. Power Sources* **2012**, *209*, 52–56.

(14) Ding, C.; Nohira, T.; Kuroda, K.; Hagiwara, R.; Fukunaga, A.; Sakai, S.; Nitta, K.; Inazawa, S. NaFSA–C_1C_3pyrFSA Ionic Liquids for Sodium Secondary Battery Operating over a Wide Temperature Range. *J. Power Sources* **2013**, *238*, 296–300.

(15) Matsumoto, K.; Okamoto, Y.; Nohira, T.; Hagiwara, R. Thermal and Transport Properties of $Na[N(SO_2F)_2]$–[*N*-Methyl-*N*-propylpyrrolidinium][$N(SO_2F)_2$] Ionic Liquids for Na Secondary Batteries. *J. Phys. Chem. C* **2015**, *119*, 7648−7655.

(16) Matsumoto, K.; Hosokawa, T.; Nohira, T.; Hagiwara, R.; Fukunaga, A.; Numata, K.; Itani, E.; Sakai, S.; Nitta, K.; Inazawa, S. The Na[FSA]–[C_2C_1im][FSA] ($C_2C_1im^+$:1-ethyl-3-methylimidazolium and FSA^-:bis(fluorosulfonyl)amide) Ionic Liquid Electrolytes for Sodium Secondary Batteries. *J. Power Sources* **2014**, *265*, 36–39.

(17) Taylor, S. R.; McLennan, S. M. *The Continental Crust: its Composition and Evolution*; Blackwell Scientific Publication, Oxford, UK, **1985**.

(18) Marcus, Y. Thermodynamic Functions of Transfer of Single Ions from Water to Nonaqueous and Mixed Solvents, PART 3: STANDARD POTENTIALS OF SELECTED ELECTRODES. *Pure & Appl. Chem.* **1985**, *57*, 1129–1132.

(19) Komaba, S.; Hasegawa, T.; Dahbi, M.; Kubota, K. Potassium Intercalation into Graphite to Realize High-Voltage/High-Power Potassium-Ion Batteries and Potassium-Ion Capacitors. *Electrochem. Commun.* **2015**, *60*, 172–175.

(20) Kasajima, T.; Nishikiori, T.; Nohira, T.; Ito, Y. Electrochemical Window and the Characteristics of (α + β) Al–Li Alloy Reference Electrode for a LiBr–KBr–CsBr Eutectic Melt. *J. Electrochem. Soc.* **2004**, *151*, E335–E339.

(21) Watarai, A.; Kubota, K.; Yamagata, M.; Goto, T.; Nohira, T.; Hagiwara, R.; Ui, K.; Kumagai, N. A Rechargeable Lithium Metal Battery Operating at Intermediate Temperatures Using Molten Alkali Bis(trifluoromethylsulfonyl)amide Mixture as an Electrolyte. *J. Power Sources* **2008**, *183*, 724–729.

(22) Kubota, K.; Tamaki, K.; Nohira, T.; Goto, T.; Hagiwara, R. Electrochemical Properties of Alkali Bis(trifluoromethylsulfonyl)amides and Their Eutectic Mixtures. *Electrochim. Acta* **2010**, *55*, 1113–1119.

(23) Okoshi, M.; Yamada, Y.; Komaba, S.; Yamada, A.; Nakai, H. Theoretical Analysis of Interactions between Potassium Ions and Organic Electrolyte Solvents: A Comparison with Lithium, Sodium, and Magnesium Ions. *J. Electrochem. Soc.* **2017**, *164*, A54–A60.

(24) Massalski, T. B. *Binary Alloy Phase Diagrams*, 2nd ed.; ASM International: Ohio, US, **1990**.

(25) Eftekhari, A.; Jian, Z.; Ji, X. Potassium Secondary Batteries. *ACS Appl. Mater. Interfaces* **2017**, *9*, 4404–4419.

(26) Pramudita, J. C.; Sehrawat, D.; Goonetilleke, D.; Sharma, N. An Initial Review of the Status of Electrode Materials for Potassium-Ion Batteries. *Adv. Energy Mater*. **2017**, DOI: 10.1002/aenm.201602911.

(27) Itaya, K.; Ataka, T.; Toshima, S. Spectroelectrochemistry and Electrochemical Preparation Method of Prussian Blue Modified Electrodes. *J. Am. Chem. Soc.* **1982**, *104,* 4767–4772.

(28) Eftekhari, A. A High-Voltage Solid-State Secondary Cell Based on Chromium Hexacyanometallates. *J. Power Sources* **2003**, *117*, 249–254.

(29) Wessells, C. D.; Huggins, R. A.; Cui, Y. Copper Hexacyanoferrate Battery Electrodes with Long Cycle Life and High Power. *Nat. Commun.* **2011**, *2*, 550.

(30) Wessells, C. D.; Peddada, S. V.; McDowell, M. T.; Huggins, R. A.; Cui, Y. The Effect of Insertion Species on Nanostructured Open Framework Hexacyanoferrate Battery Electrodes. *J. Electrochem. Soc.* **2012**, *159*, A98–A103.

(31) Su, D.; McDonagh, A.; Qiao, S.-Z.; Wang, G. High-Capacity Aqueous Potassium-Ion Batteries for Large-Scale Energy Storage. *Adv. Mater.* **2017**, DOI: 10.1002/adma.201604007.

(32) Eftekhari, A. Potassium Secondary Cell Based on Prussian Blue Cathode. *J. Power Sources*, **2004**, *126*, 221–228.

(33) Zhang, C. L.; Dong, H. S.; Wu, M. H.; Yang, Y.; Lei, Y. Potassium Prussian Blue Nanoparticles: A Low-Cost Cathode Material for Potassium-Ion Batteries. *Adv. Funct. Mater.* **2017**, DOI: 10.1002/adfm.201604307.

(34) Bie, X.; Kubota, K.; Hosaka, T.; Chihara, K.; Komaba, S. A Novel K-Ion Battery: Hexacyanoferrate(II)/Graphite Cell. *J. Mater. Chem. A* **2017**, *5*, 4325–4330.

(35) Vaalma, C.; Giffin, G. A.; Buchholz, D.; Passerini, S. Non-Aqueous K-Ion Battery Based on Layered $K_{0.3}MnO_2$ and Hard Carbon/Carbon Black. *J. Electrochem. Soc.* **2016**, *163*, A1295–A1299.

(36) Wang, X.; Xu, X.; Niu, C.; Meng, J.; Huang, M.; Liu, X.; Liu, Z.; Mai, L. Earth Abundant Fe/Mn-Based Layered Oxide Interconnected Nanowires for Advanced K-Ion Full Batteries. *Nano Lett.* **2017**, *17*, 544–550.

(37) Hironaka, Y.; Kubota, K.; Komaba, S. P2- and P3-K_xCoO_2 as an Electrochemical Potassium Intercalation Host. *Chem. Commun.* **2017**, *53*, 3693–3696.

(38) Mathew, V.; Kim, S.; Kang, J.; Gim, J.; Song, J.; Baboo, J. P.; Park, W.; Ahn, D.; Han, J.; Gu, L.; et al. Amorphous Iron Phosphate: Potential Host for Various Charge Carrier Ions. *NPG Asia Materials* **2014**, *6*, e138.

(39) Nikitina, V. A.; Fedotov, S. S.; Vassiliev, S. Y.; Samarin, A. S.; Khasanova, N. R.; Antipov, E. V. Transport and Kinetic Aspects of Alkali Metal Ions Intercalation into $AVPO_4F$ Framework. *J. Electrochem. Soc.* **2017**, *164*, A6373–A6380.

(40) Han, J.; Li, G.-N.; Liu, F.; Wang, M.; Zhang, Y.; Hu, L.; Dai, C.; Xu, M. Investigation of $K_3V_2(PO_4)_3$/C Nanocomposites as High-Potential Cathode Materials for Potassium-Ion Batteries. *Chem. Commun.* **2017**, *53*, 1805–1808.

(41) Chihara, K.; Katogi, A.; Kubota, K.; Komaba, S. $KVPO_4F$ and $KVOPO_4$ toward 4 Volt-Class Potassium-Ion Batteries. *Chem. Commun.* **2017**, *53*, 5208–5211.

(42) Recham, N.; Rousse, G.; Sougrati, M. T.; Chotard, J.-N.; Frayret, C.; Mariyappan, S.; Melot, B. C.; Jumas, J.-C.; Tarascon, J.-M. Preparation and Characterization of a Stable $FeSO_4F^-$ Based Framework for Alkali Ion Insertion Electrodes. *Chem. Mater.* **2012**, *24*, 4363–4370.

(43) Luo, W.; Wan, J.; Ozdemir, B.; Bao, W.; Chen, Y.; Dai, J.; Lin, H.; Xu, Y.; Gu, F.; Barone, V.; et al. Potassium Ion Batteries with Graphitic Materials. *Nano Lett.* **2015**, *15*, 7671–7677.

(44) Jian, Z.; Luo, W.; Ji, X. Carbon Electrodes for K-Ion Batteries. *J. Am. Chem. Soc.* **2015**, *137*, 11566–11569.

(45) Zhao, J.; Zou, X.; Zhu, Y.; Xu, Y.; Wang, C. Electrochemical Intercalation of Potassium into Graphite. *Adv. Funct. Mater.* **2016**, *26*, 8103–8110.

(46) Xing, Z.; Qi, Y.; Jian, Z.; Ji, X. Polynanocrystalline Graphite: A New Carbon Anode with Superior Cycling Performance for K-Ion Batteries. *ACS Appl. Mater. Interfaces* **2017**, *9*, 4343–4351.

(47) Jian, Z.; Xing, Z.; Bommier, C.; Li, Z.; Ji, X. Hard Carbon Microspheres: Potassium-Ion Anode Versus Sodium-Ion Anode. *Adv. Energy Mater*. **2016**, DOI: 10.1002/aenm.201501874.

(48) Sultana, I; Ramireddy, T.; Rahman, M. M.; Chen, Y.; Glushenkov, A. M. Tin-Based Composite Anodes for Potassium-Ion Batteries. *Chem. Commun.* **2016**, *52*, 9279–9282.

(49) Zhang, W.; Mao, J.; Li, S.; Chen, Z.; Guo, Z. Phosphorus-Based Alloy Materials for Advanced Potassium-Ion Battery Anode. *J. Am. Chem. Soc.* **2017**, *139*, 3316–3319.

(50) McCulloch, W. D.; Ren, X.; Yu, M.; Huang, Z.; Wu, Y. Potassium-Ion Oxygen Battery Based on a High Capacity Antimony Anode. *ACS Appl. Mater. Interfaces* **2015**, *7*, 26158–26166.

(51) Han, J.; Xu, M.; Niu, Y.; Li, G.-N.; Wang, M.; Zhang, Y.; Jia, M.; Li, C. M. Exploration of $K_2Ti_8O_{17}$ as an Anode Material for Potassium-Ion Batteries. *Chem. Commun.* **2016**, *52*, 11274–11276.

(52) Han, J.; Niu, Y.; Bao, S.-J.; Yu, Y.-N.; Lu, S.-Y.; Xu, M. Nanocubic $KTi_2(PO_4)_3$ Electrodes for Potassium-Ion Batteries. *Chem. Commun.* **2016**, *52*, 11661–11664.

(53) Iwasaki, K.; Yoshii, K.; Tsuzuki, S.; Matsumoto, H.; Tsuda, T.; Kuwabata, S. Alkali Metal Salts with Designable Aryltrifluoroborate Anions. *J. Phys. Chem. B* **2016**, *120*, 9468–9476.

(54) Guerfi, A.; Duchesne, S.; Kobayashi, Y.; Vijh, A.; Zaghib, K. $LiFePO_4$ and Graphite Electrodes with Ionic Liquids Based on Bis(fluorosulfonyl)imide $(FSI)^-$ for Li-Ion Batteries. *J. Power Sources* **2008**, *175*, 866–873.

(55) Bhatt, A. I.; Best, A. S.; Huang, J.; Hollenkamp, A. F. Application of the *N*-propyl-*N*-methyl-pyrrolidinium Bis(fluorosulfonyl)imide RTIL Containing Lithium Bis(fluorosulfonyl)imide in Ionic Liquid Based Lithium Batteries. *J. Electrochem. Soc.* **2010**, *157*, A66–A74.

(56) Yoon, H.; Best, A. S.; Forsyth, M.; MacFarlane, D. R.; Howlett, P. C. Physical Properties of High Li-Ion Content *N*-propyl-*N*-methylpyrrolidinium Bis(fluorosulfonyl)imide Based Ionic Liquid Electrolytes. *Phys. Chem. Chem. Phys.* **2015**, *17*, 4656–4663.

(57) Piper, D. M.; Evans, T.; Leung, K.; Watkins, T.; Olson, J.; Kim, S. C.; Han, S. S.; Bhat, V.; Oh, K. H.; Buttry, D. A.; et al. Stable Silicon-Ionic Liquid Interface for Next-Generation Lithium-Ion Batteries. *Nat. Commun.* **2015**, *6*, 6230.

(58) Easteal, A. J.; Angell, C. A. Viscosity of Molten $ZnCl_2$ and Supercritical Behavior in Its Binary Solutions. *J. Chem. Phys.* **1972**, *56*, 4231–4233.

(59) Xu, W.; Cooper, E. I.; Angell, C. A. Ionic Liquids: Ion Mobilities, Glass Temperatures, and Fragilities. *J. Phys. Chem. B* **2003**, *107*, 6170–6178.

(60) Xu, W.; Angell, C. A. Solvent-Free Electrolytes with Aqueous Solution-Like Conductivities. *Science* **2003**, *302*, 422–425.

(61) Pugsley, F. A.; Westmore, F. E. W. Molten Salts: Viscosity of Silver Nitrate. *Can. J. Chem.* **1954**, *32*, 839–841.

(62) Schreiner, C.; Zugmann, S.; Hartl, R.; Gores, H. J. Fractional Walden Rule for Ionic Liquids: Examples from Recent Measurements and a Critique of the So-Called Ideal KCl Line for the Walden Plot. *J. Chem. Eng. Data* **2010**, *55*, 1784–1788.

(63) Makino, T.; Kanakubo, M.; Umecky, T.; Suzuki, A.; Nishida, T.; Takano, J. Electrical Conductivities, Viscosities, and Densities of *N*-Methoxymethyl- and *N*-Butyl-*N*-methylpyrrolidinium Ionic Liquids with the Bis(fluorosulfonyl)amide Anion. *J. Chem. Eng. Data* **2012**, *57*, 751–755.

Table 1 DSC transition temperatures (K) for the K[FSA]–[C_3C_1pyrr][FSA] system.[a]

x(K[FSA])	$T_{m\_o}(1)$	$T_{m\_e}(1)$	$T_{m\_o}(2)$	$T_{m\_e}(2)$	T_{tr_o}	T_g
0	264	269			191	
					253	
0.05	240	264			192	
					254	
0.10	239	261	230	n.d.	191	
					252	
0.15	240	258	231	n.d.	191	
0.20	238	256	230	n.d.	191	176
0.25	241	253	232	n.d.	192	178
0.30	240	355	230	n.d.	192	182
0.40	n.d.	364				189
0.50	n.d.	365				195
0.60	242	368	232	n.d.	191	198
0.70	238	371	228	322	191	182
0.80	240	371	230	329	190	
0.90	244	373	230	n.d.	190	
1	375	380				

[a] $T_{m\_o}(1)$: onset temperatures of melting for stable phases, $T_{m\_e}(1)$: end temperatures of melting for stable phases, $T_{m\_o}(2)$: onset temperatures of melting for metastable phases, $T_{m\_e}(2)$: end temperatures of melting for metastable phases, T_{tr_o}: onset temperatures of solid-solid transition, T_g: glass transition temperatures

Table 2 Viscosities (mPa s) of the K[FSA]–[C_3C_1pyrr][FSA] system.

T / K	x(K[FSA])					
	0	0.05	0.10	0.15	0.20	0.25
273	103	125	156	200	256	342
278	83.5	100	123	155	195	255
283	68.5	81.3	98.2	123	152	196
288	56.9	67.0	80.0	98.1	120	153
293	47.8	55.7	65.9	80.0	96.8	121
298	40.6	46.9	55.6	66.0	78.2	98.4
303	34.8	39.9	46.9	54.9	64.7	79.4
308	30.0	34.2	39.9	46.5	54.1	65.7
313	26.1	29.8	34.3	39.4	45.6	55.5
318	22.9	26.0	29.6	33.8	38.9	46.7
323	20.2	22.5	25.8	29.1	33.4	39.8
328	17.8	19.8	22.6	25.4	28.9	33.6
333	15.9	17.5	19.8	22.2	25.1	29.3
338	14.2	15.6	17.5	19.6	22.0	25.4
343	12.8	14.0	15.6	17.3	19.4	22.2
348	11.5	12.6	14.0	15.5	17.2	19.8
353	10.5	11.4	12.7	13.9	15.4	17.6
358	9.6	10.3	11.5	12.5	13.8	15.6
363	8.8	9.4	10.4	11.3	12.5	14.1
368	8.1	8.7	9.6	10.4	11.4	12.8
373	7.6	8.0	8.8	9.5	10.4	11.5
378	7.0	7.4	8.1	8.8	9.5	10.5
383	6.5	6.9	7.4	8.1	8.7	9.6
388	6.1	6.4	6.9	7.5	8.0	8.8
393	5.7	6.0	6.5	6.9	7.4	8.2

Table 3 Ionic conductivities (mS cm^{-1}) of the K[FSA]–[C_3C_1pyrr][FSA] system.

T / K	x(K[FSA])					
	0	0.05	0.10	0.15	0.20	0.25
258	–	–	–	–	0.63	0.45
263	–	–	1.5	1.2	0.88	0.65
268	–	2.3	1.9	1.5	1.2	0.91
273	3.5	2.9	2.5	2.0	1.6	1.2
278	4.3	3.6	3.1	2.6	2.1	1.6
283	5.2	4.4	3.8	3.2	2.6	2.1
288	6.2	5.3	4.7	3.9	3.2	2.6
293	7.2	6.3	5.6	4.8	4.0	3.3
298	8.4	7.3	6.6	5.7	4.8	4.0
303	9.7	8.5	7.7	6.7	5.7	4.8
308	11.0	9.8	8.9	7.8	6.7	5.7
313	12.5	11.1	10.2	9.1	7.9	6.8
318	14.0	12.6	11.6	10.4	9.1	7.9
323	15.6	14.2	13.1	11.8	10.4	9.1
328	17.4	15.8	14.7	13.3	11.8	10.4
333	19.2	17.6	16.4	15.0	13.3	11.8
338	21.2	19.4	18.2	16.7	15.0	13.3
343	23.2	21.3	20.1	18.5	16.7	15.0
348	25.3	23.4	22.1	20.4	18.5	16.6
353	27.5	25.5	24.2	22.4	20.4	18.6
358	29.8	27.7	26.4	24.5	22.4	20.5
363	32.2	30.1	28.7	26.8	24.6	22.4
368	34.7	32.5	31.0	29.0	26.7	24.2
373	37.4	35.0	33.4	31.4	29.0	26.1
378	40.1	37.7	36.0	33.8	31.4	28.7
383	43.0	40.5	38.8	36.3	33.8	31.2
388	46.1	43.5	41.5	38.8	36.3	33.6
393	49.5	46.7	44.3	41.4	38.8	35.9

Table 4 Densities (g cm^{-3}) of the K[FSA]–[C_3C_1pyrr][FSA] system.[a]

T / K	x(K[FSA])					
	0	0.05	0.10	0.15	0.20	0.25
278	1.3553	1.3740	1.3935	1.4146	1.4370	1.4610
283	1.3512	1.3698	1.3893	1.4103	1.4326	1.4566
288	1.3472	1.3657	1.3851	1.4061	1.4284	1.4522
293	1.3431	1.3616	1.3810	1.4019	1.4241	1.4479
298	1.3391	1.3575	1.3769	1.3977	1.4198	1.4436
303	1.3351	1.3535	1.3727	1.3935	1.4156	1.4393
308	1.3311	1.3495	1.3687	1.3894	1.4114	1.4350
313	1.3272	1.3454	1.3646	1.3852	1.4072	1.4308
318	1.3232	1.3414	1.3605	1.3811	1.4031	1.4266
323	1.3193	1.3375	1.3565	1.3771	1.3989	1.4224
328	1.3153	1.3335	1.3525	1.3730	1.3948	1.4182
333	1.3114	1.3296	1.3485	1.3689	1.3907	1.4140
338	1.3076	1.3256	1.3445	1.3649	1.3866	1.4098
343	1.3038	1.3217	1.3406	1.3609	1.3825	1.4057
348	1.3000	1.3178	1.3366	1.3569	1.3784	1.4016
353	1.2962	1.3139	1.3327	1.3529	1.3744	1.3975
358	1.2924	1.3101	1.3288	1.3489	1.3703	1.3934
363	1.2887	1.3063	1.3250	1.3450	1.3664	1.3893
$A_\rho\times10^4$	–7.8479	–7.9634	–8.0648	–8.1851	–8.3037	–8.4272
B_ρ	1.5732	1.5950	1.6174	1.6418	1.6675	1.6949

[a] Density values were fitted by the following equation; $\rho = A_\rho T + B_\rho$

Table 5 Molar concentrations (mol dm^{-3}) of the K[FSA]–[C_3C_1pyrr][FSA] system.

T / K	x(K[FSA])					
	0	0.05	0.10	0.15	0.20	0.25
278	0	0.2260	0.4653	0.7192	0.9891	1.2766
283	0	0.2254	0.4639	0.7171	0.9861	1.2728
288	0	0.2247	0.4625	0.7149	0.9832	1.2690
293	0	0.2240	0.4611	0.7128	0.9802	1.2652
298	0	0.2233	0.4598	0.7106	0.9773	1.2614
303	0	0.2227	0.4584	0.7085	0.9744	1.2577
308	0	0.2220	0.4570	0.7064	0.9715	1.2539
313	0	0.2213	0.4557	0.7043	0.9686	1.2502
318	0	0.2207	0.4543	0.7022	0.9658	1.2466
323	0	0.2200	0.4530	0.7002	0.9629	1.2429
328	0	0.2194	0.4516	0.6981	0.9601	1.2392
333	0	0.2187	0.4503	0.6960	0.9572	1.2356
338	0	0.2181	0.4490	0.6940	0.9544	1.2319
343	0	0.2174	0.4476	0.6919	0.9516	1.2283
348	0	0.2168	0.4463	0.6899	0.9488	1.2247
353	0	0.2162	0.4450	0.6879	0.9460	1.2211
358	0	0.2155	0.4437	0.6858	0.9432	1.2175
363	0	0.2149	0.4424	0.6839	0.9405	1.2140

Table 6 The α values of K[FSA]–[C_3C_1pyrr][FSA] ionic liquid in the Walden plot.

	x(K[FSA])					
	0	0.05	0.10	0.15	0.20	0.25
α	0.911	0.912	0.915	0.912	0.917	0.921

Table 7 Summary of electrochemical windows for M[FSA]–[C_3C_1pyrr][FSA] ionic liquids (M = K, Na, or Li).[a]

	Limit potential / V vs. Fc^+/Fc		Electrochemical window / V
	Cathode	Anode	
K-ion system	–3.31	2.41	5.72
Na-ion system	–2.96	2.46	5.42
Li-ion system	–3.07	2.41	5.48

[a] Anode limits are the potentials where the current density reaches 0.1 mA cm^{-2} in the anodic sweep.

Table 8 Comparison of the standard potentials of M^+/M (M = K, Na, or Li) in various electrolytes at 298 K.*

Electrolyte	Difference of standard potential / V		Reference
	$E^\circ(K^+/K) - E^\circ(Na^+/Na)$	$E^\circ(K^+/K) - E^\circ(Li^+/Li)$	
M[FSA]–[C_3C_1pyrr][FSA]**	–0.35	–0.24	This study
Water	–0.22	0.10	18
PC	–0.32	–0.09	18
MeCN	–0.32	–0.15	18
DMF	–0.23	0.10	18
DMSO	–0.22	0.13	18
TMS	–0.23	N.A.	18

PC = Propylene carbonate, MeCN = Acetonitrile, DMF = *N*,*N*-Dimethylformamide, DMSO = Dimethyl sulfoxide, TMS = Tetramethylene sulfone (sulfolane)

* The standard concentration is 1 mol dm^{-3}.

** Values of M[FSA]–[C_3C_1pyrr][FSA] were measured at the molar concentration of M[FSA] of 0.98 mol dm^{-3} for K[FSA] (this study), 0.98 mol dm^{-3} for Na[FSA][15], and 1.0 mol dm^{-3} for Li[FSA][56].

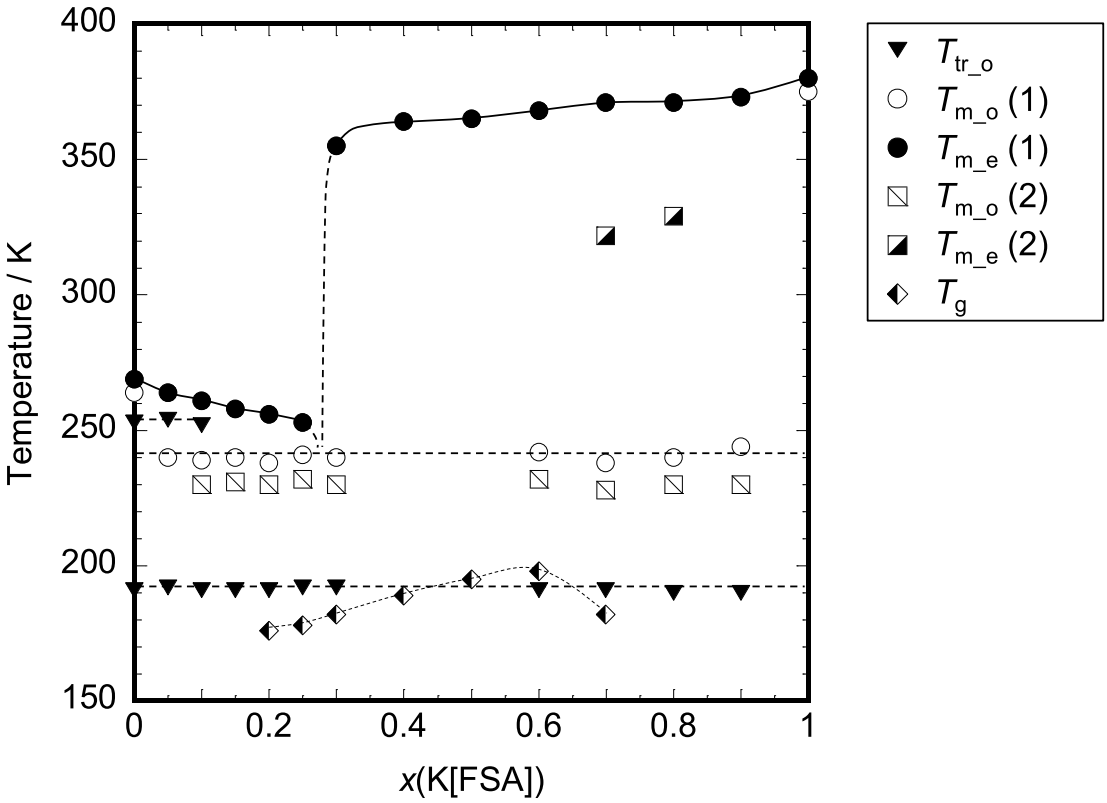

Figure 1 Phase diagram of the K[FSA]–[C_3C_1pyrr][FSA] system. $T_{m\_o}(1)$: onset temperatures of melting for stable phases, $T_{m\_e}(1)$: end temperatures of melting for stable phases, $T_{m\_o}(2)$: onset temperatures of melting for metastable phases, $T_{m\_e}(2)$: end temperatures of melting for metastable phases, T_{tr_o}: onset temperatures of solid-solid transition, T_g: glass transition temperatures.

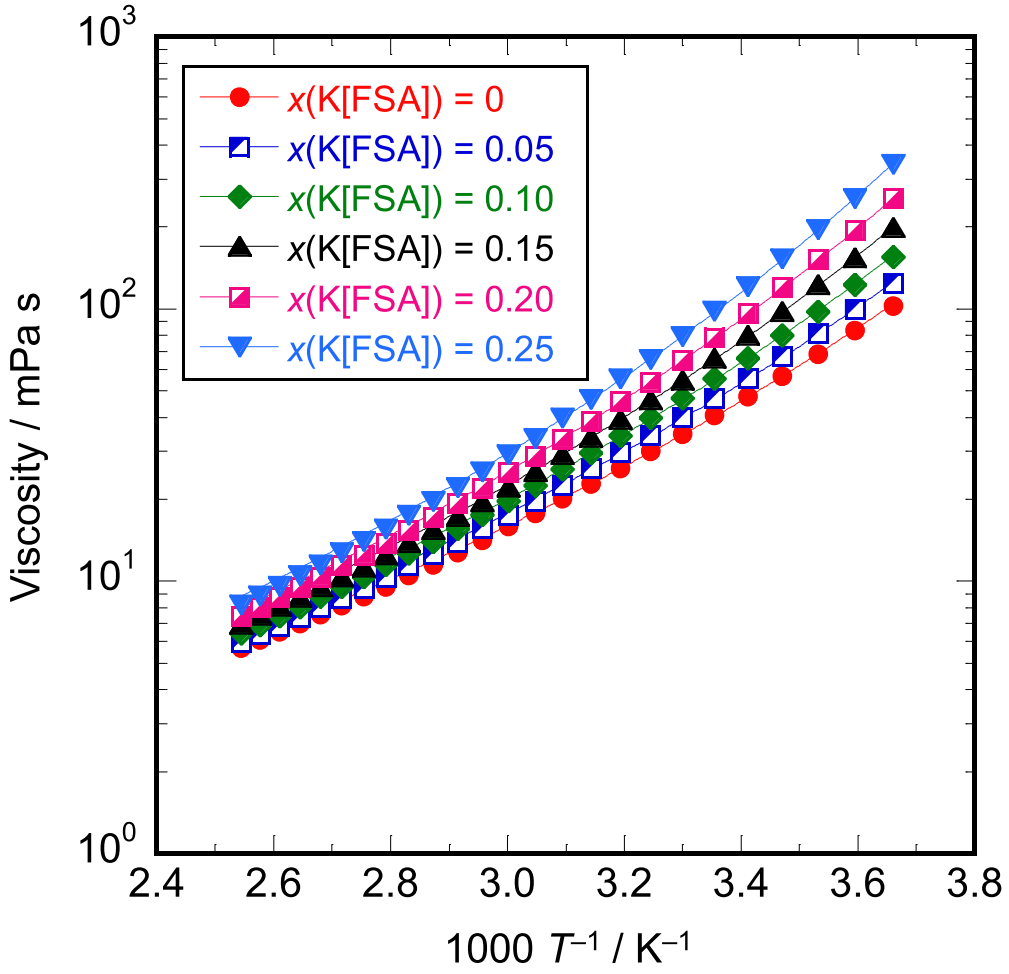

Figure 2 Arrhenius plots of viscosities for the K[FSA]–[C_3C_1pyrr][FSA] system (x(K[FSA] = 0–0.25).

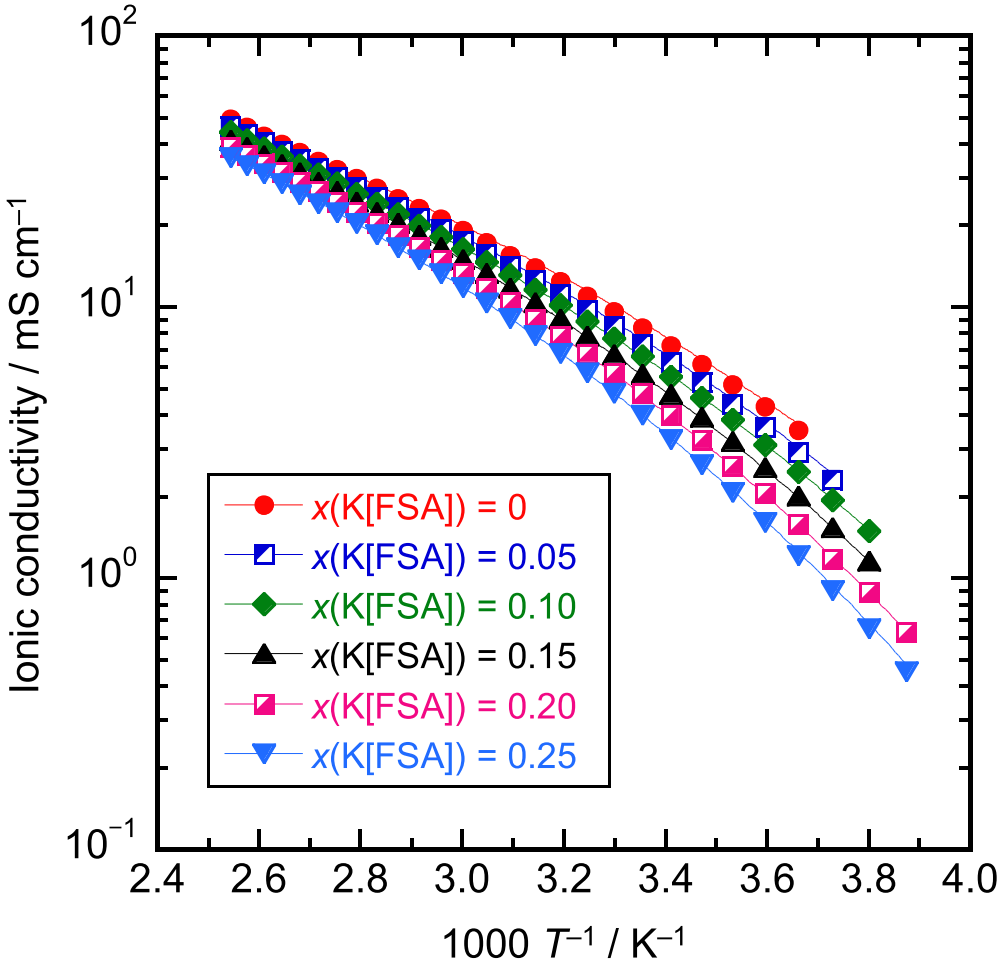

Figure 3 Arrhenius plots of ionic conductivities for the K[FSA]–[C_3C_1pyrr][FSA] system (x(K[FSA] = 0–0.25).

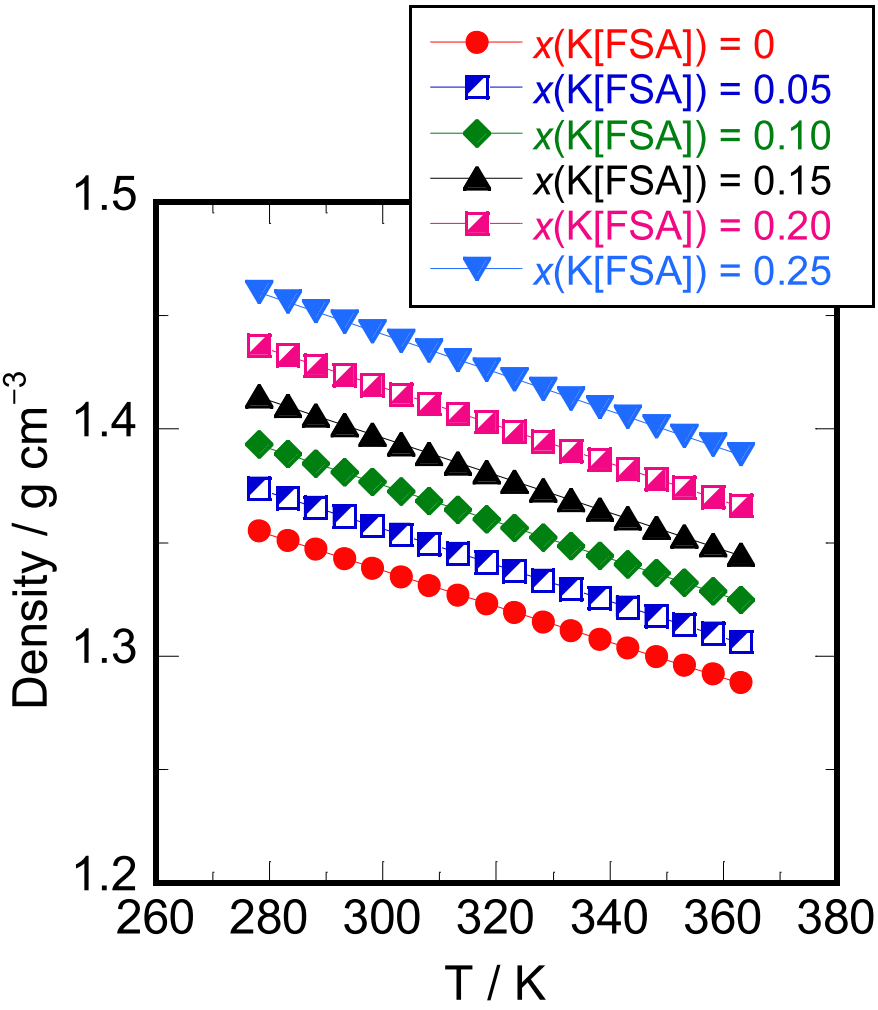

Figure 4 Density plots of the K[FSA]–[C_3C_1pyrr][FSA] system (x(K[FSA] = 0–0.25).

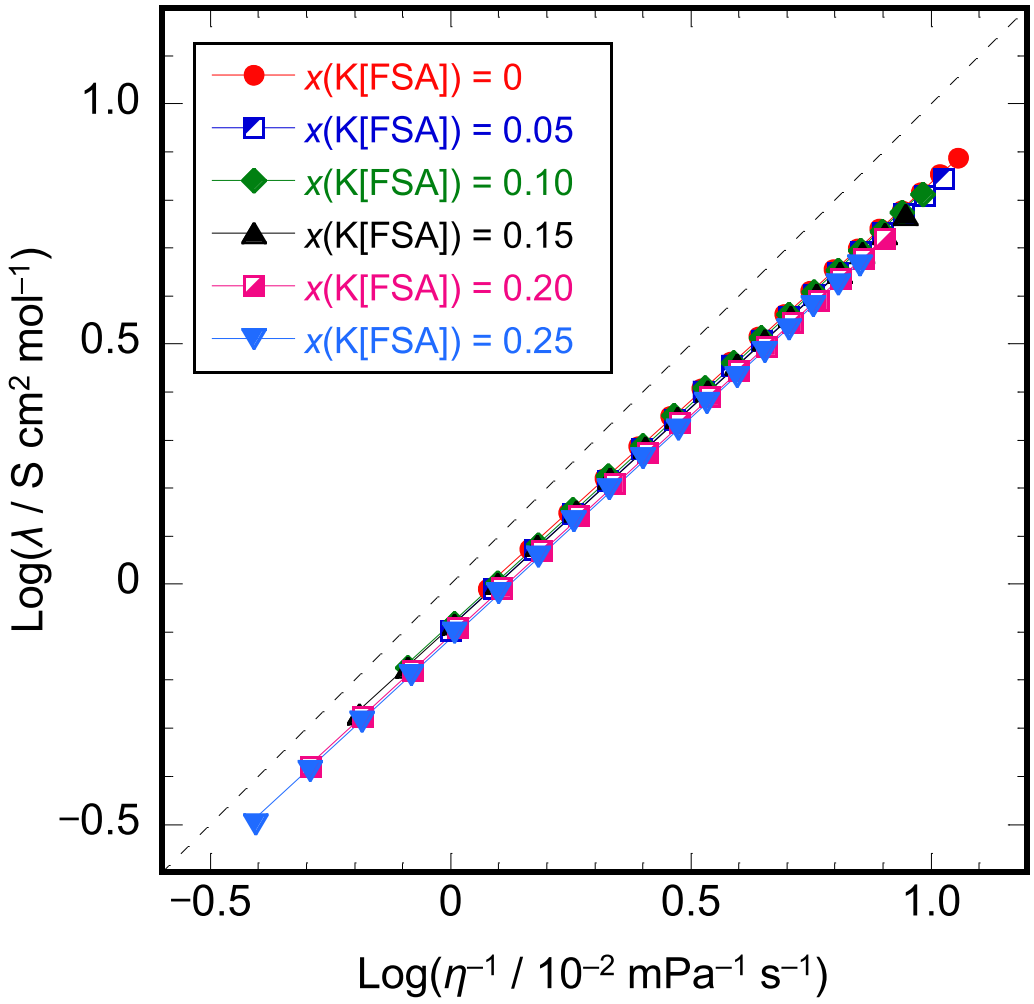

Figure 5 Walden plots of the K[FSA]–[C_3C_1pyrr][FSA] system (x(K[FSA] = 0–0.25). The ideal KCl line is indicated by a dashed line.

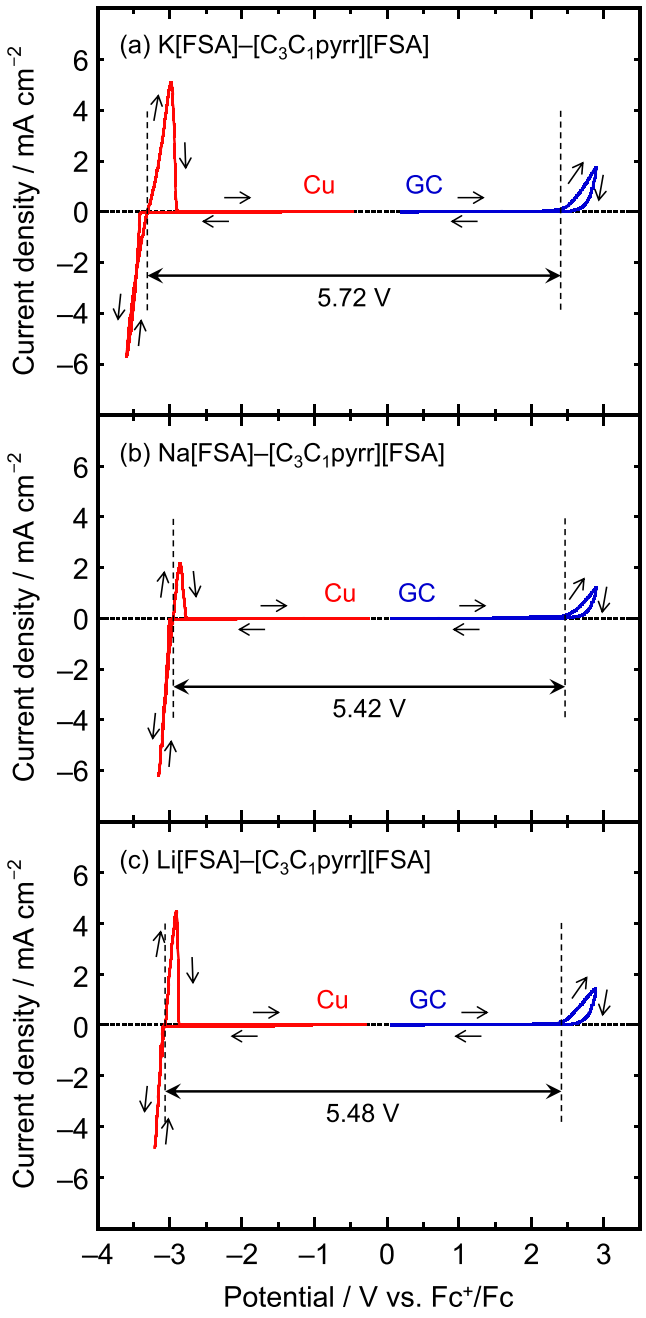

Figure 6 Cyclic voltammograms of (a) K[FSA]–[C_3C_1pyrr][FSA] (x(K[FSA]) = 0.20), (b) Na[FSA]–[C_3C_1pyrr][FSA] (x(Na[FSA]) = 0.20), (c) Li[FSA]–[C_3C_1pyrr][FSA] (x(Li[FSA]) = 0.20) at 298 K. Working electrodes: copper disk (cathode limit) and glassy carbon disk (anodic limit). Scan rate: 5 mV s^{-1}. Cycle number: 1st. Cathode and anode limits of each electrolyte are indicated by dashed lines.

TOC Graphic

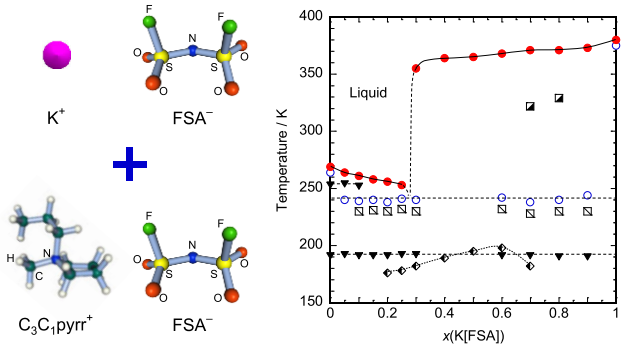
K+
FSA−
C3C1pyrr+
FSA−
Liquid
Temperature / K
x(K[FSA])
400
350
300
250
200
150
0
0.2
0.4
0.6
0.8
1

Supporting Information

Physicochemical and Electrochemical Properties of K[$N(SO_2F)_2$]–[*N*-Methyl-*N*-propylpyrrolidinium][$N(SO_2F)_2$] Ionic Liquids for Potassium-Ion Batteries

Takayuki Yamamoto,[*,†] Kazuhiko Matsumoto,[‡,§] Rika Hagiwara,[‡,§] and Toshiyuki Nohira[*,†,§]

†Institute of Advanced Energy, Kyoto University, Uji 611-0011, Japan

‡Graduate School of Energy Science, Kyoto University, Sakyo-ku, Kyoto 606-8501, Japan

§Unit of Elements Strategy Initiative for Catalysts & Batteries (ESICB), Kyoto University, Katsura, Kyoto 615-8510, Japan

Corresponding Authors

*E-mail: yamamoto.takayuki.2w@kyoto-u.ac.jp, Tel: +81-774-38-3498, Fax: +81-774-38-3499 (Takayuki Yamamoto).

*E-mail: nohira.toshiyuki.8r@kyoto-u.ac.jp, Tel: +81-774-38-3500, Fax: +81-774-38-3499 (Toshiyuki Nohira).

Table S1 VTF parameters of viscosities for the K[FSA]–[C_3C_1pyrr][FSA] system (x(K[FSA] = 0–0.25).

x(K[FSA])	$A_\eta \times 10^3$ / mPa s $K^{-1/2}$	B_η / K	$T_{0\eta}$ / K
0	9.39	898	135
0.05	9.15	917	137
0.10	8.97	933	139
0.15	8.57	949	142
0.20	8.16	968	145
0.25	7.85	992	147

Table S2 VTF parameters of ionic conductivities for the K[FSA]–[C_3C_1pyrr][FSA] system (x(K[FSA] = 0–0.25).

x(K[FSA])	$A_\sigma \times 10^{-4}$ / mS cm^{-1} $K^{1/2}$	B_σ / K	$T_{0\sigma}$ / K
0	2.04	783	138
0.05	2.20	808	140
0.10	2.34	830	142
0.15	2.57	858	144
0.20	2.73	881	146
0.25	2.82	902	148

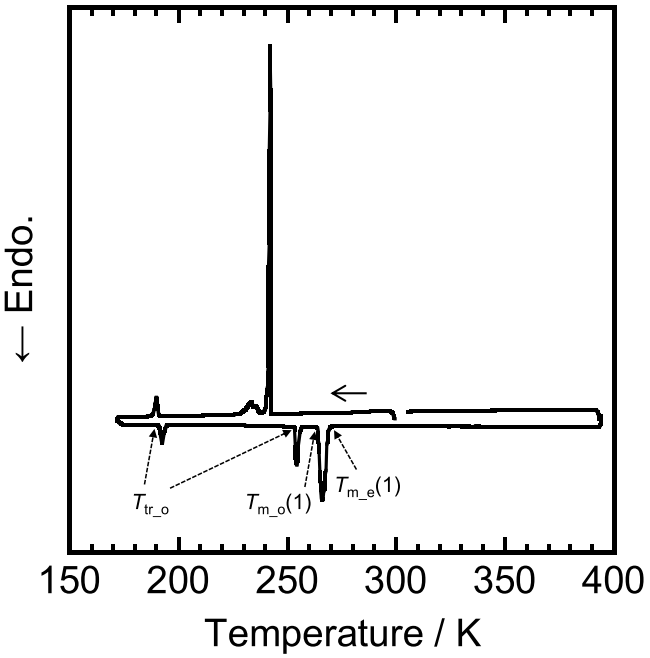

Figure S1 A DSC curve for $[C_3C_1pyrr][FSA]$. Scan rate: 2 K min^{-1}.

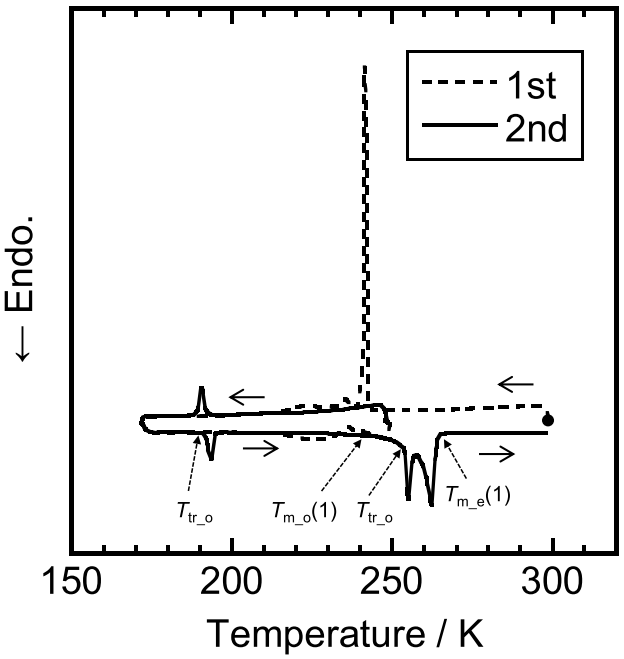

Figure S2 DSC curves for K[FSA]–$[C_3C_1pyrr][FSA]$ (x(K[FSA]) = 0.05). Scan rate: 2 K min^{-1}. Holding temperature and time before 2nd cycle: 248 K and 120 min.

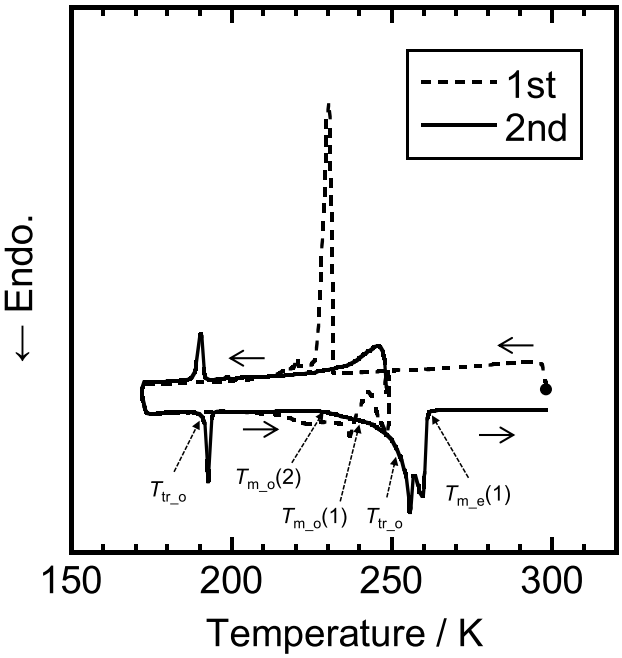

Figure S3 DSC curves for K[FSA]–[C_3C_1pyrr][FSA] (x(K[FSA]) = 0.10). Scan rate: 2 K min^{-1}. Holding temperature and time before 2nd cycle: 248 K and 120 min.

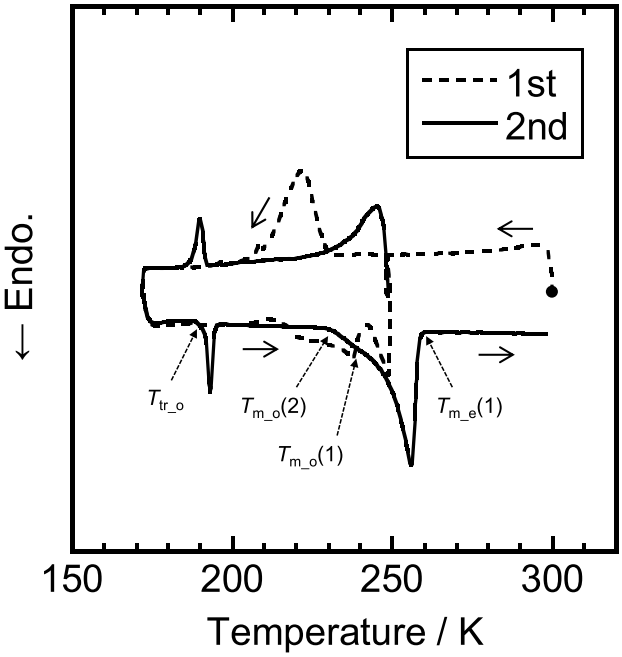

Figure S4 DSC curves for K[FSA]–[C_3C_1pyrr][FSA] (x(K[FSA]) = 0.15). Scan rate: 2 K min^{-1}. Holding temperature and time before 2nd cycle: 248 K and 120 min.

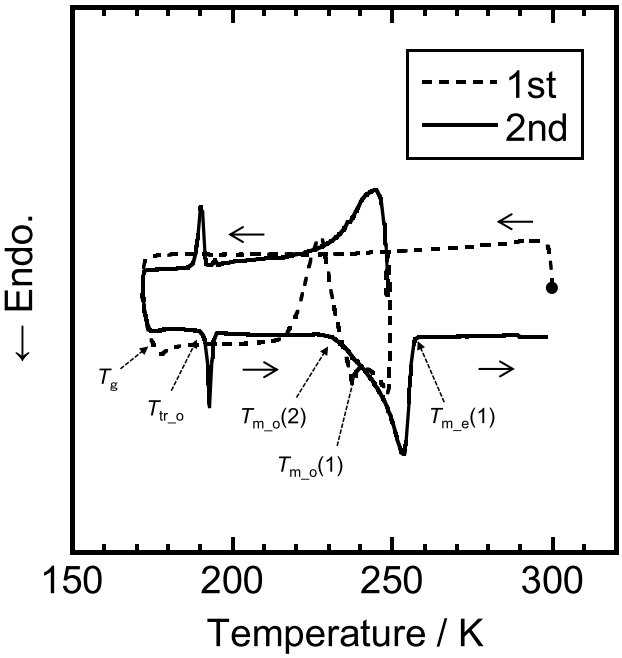

Figure S5 DSC curves for K[FSA]–[C_3C_1pyrr][FSA] (x(K[FSA]) = 0.20). Scan rate: 2 K min^{-1}. Holding temperature and time before 2nd cycle: 248 K and 120 min.

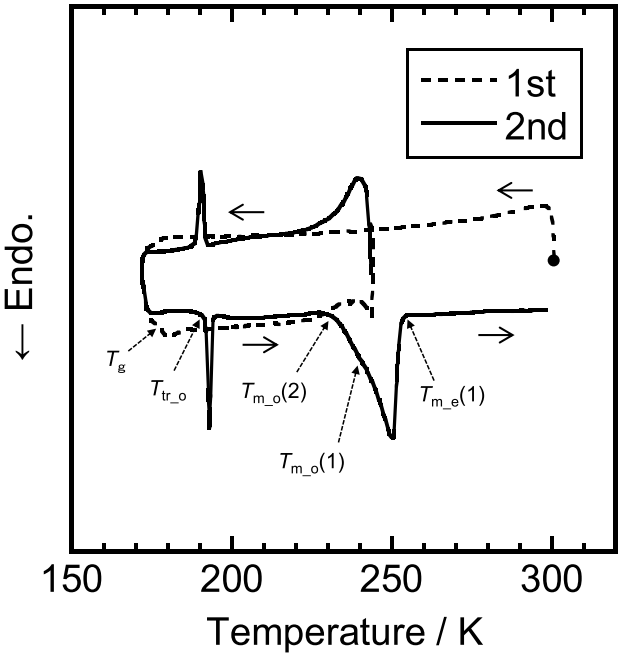

Figure S6 DSC curves for K[FSA]–[C_3C_1pyrr][FSA] (x(K[FSA]) = 0.25). Scan rate: 2 K min^{-1}. Holding temperature and time before 2nd cycle: 243 K and 120 min.

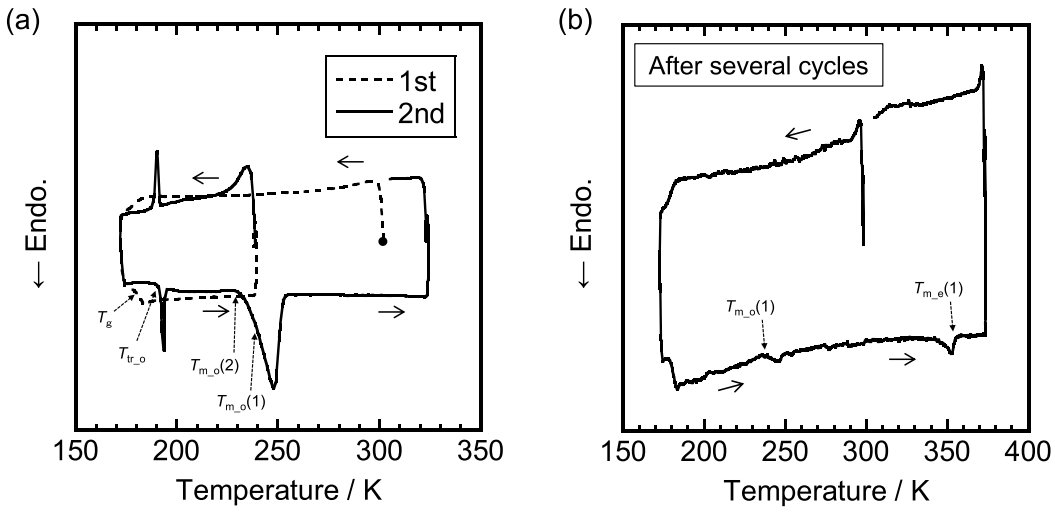

Figure S7 DSC curves for K[FSA]–[C_3C_1pyrr][FSA] (x(K[FSA]) = 0.30). Scan rates: (a) 2 K min^{-1} and (b) 1 K min^{-1}. Holding temperature and time before 2nd cycle: 238 K and 120 min.

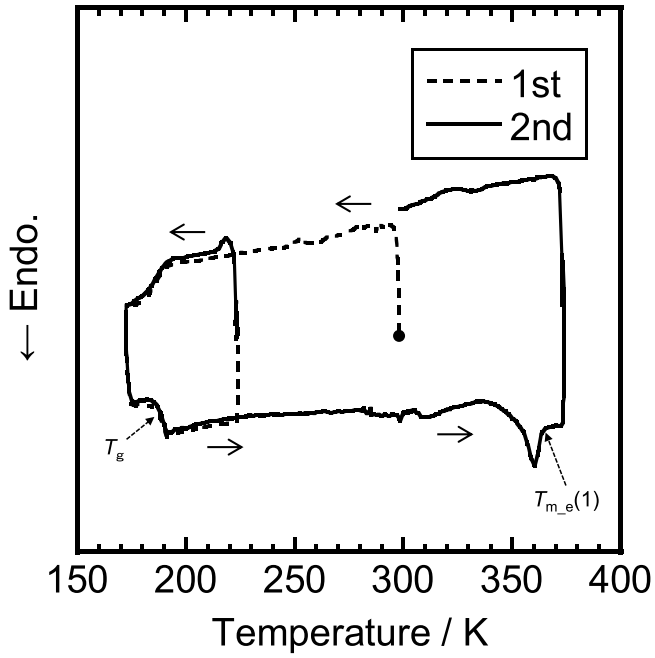

Figure S8 DSC curves for K[FSA]–[C_3C_1pyrr][FSA] (x(K[FSA]) = 0.40). Scan rate: 2 K min^{-1}. Holding temperature and time before 2nd cycle: 223 K and 120 min.

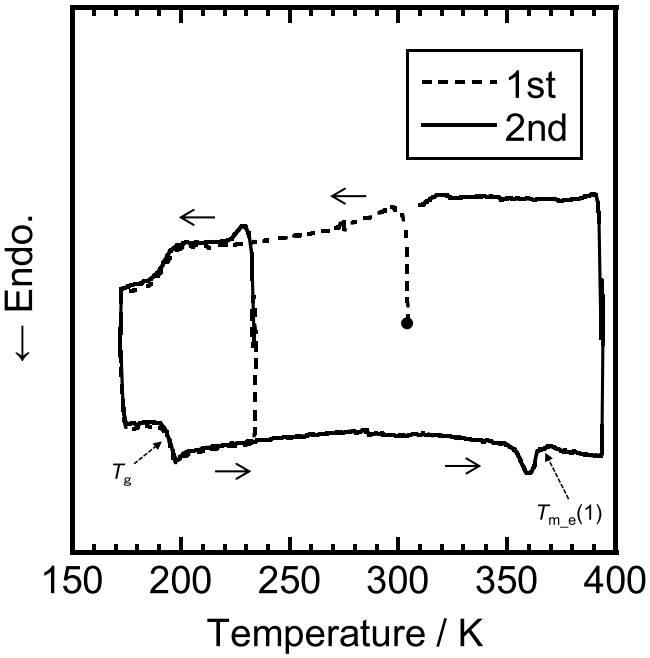

Figure S9 DSC curves for K[FSA]–[C_3C_1pyrr][FSA] (x(K[FSA]) = 0.50). Scan rate: 2 K min^{-1}. Holding temperature and time before 2nd cycle: 233 K and 60 min.

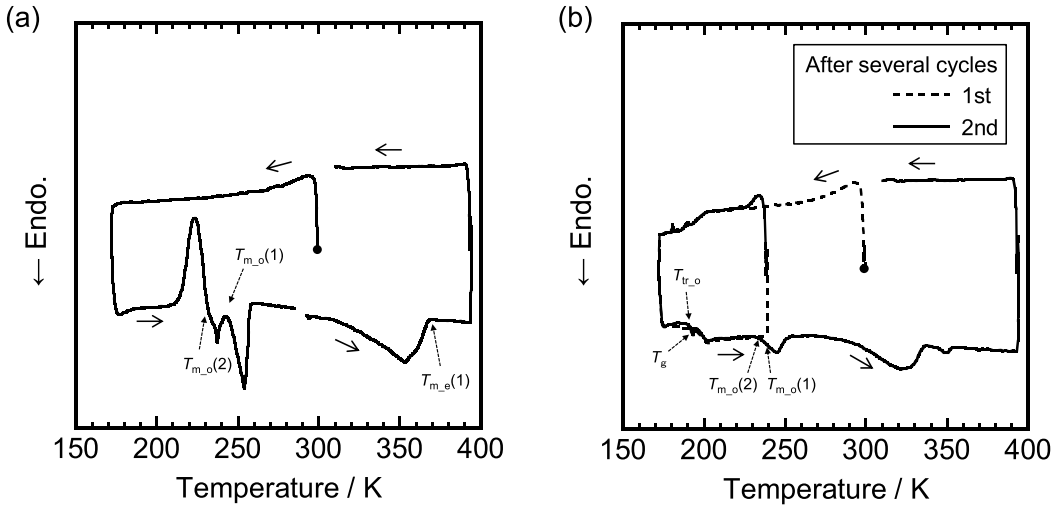

Figure S10 DSC curves for K[FSA]–[C_3C_1pyrr][FSA] (x(K[FSA]) = 0.60). Scan rate: 2 K min^{-1}. Holding temperature and time before 4th cycle: 238 K and 60 min.

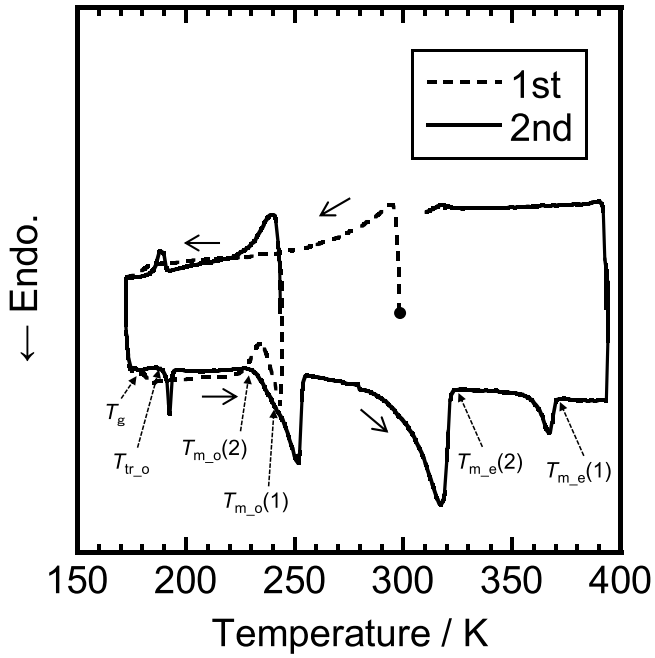

Figure S11 DSC curves for K[FSA]–[C_3C_1pyrr][FSA] (x(K[FSA]) = 0.70). Scan rate: 2 K min^{-1}. Holding temperature and time before 2nd cycle: 243 K and 60 min.

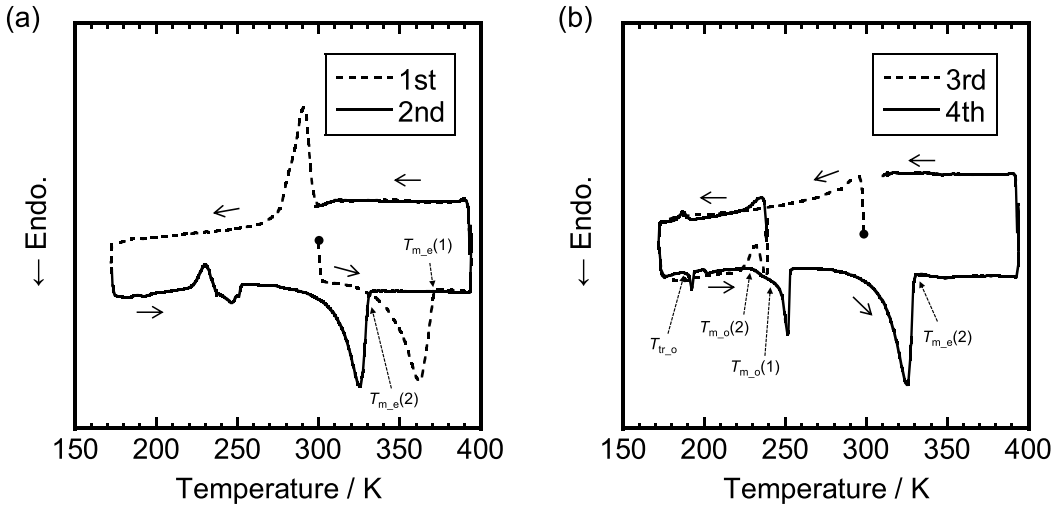

Figure S12 DSC curves for K[FSA]–[C_3C_1pyrr][FSA] (x(K[FSA]) = 0.80). Scan rate: 2 K min^{-1}. Holding temperature and time before 4th cycle: 238 K and 90 min.

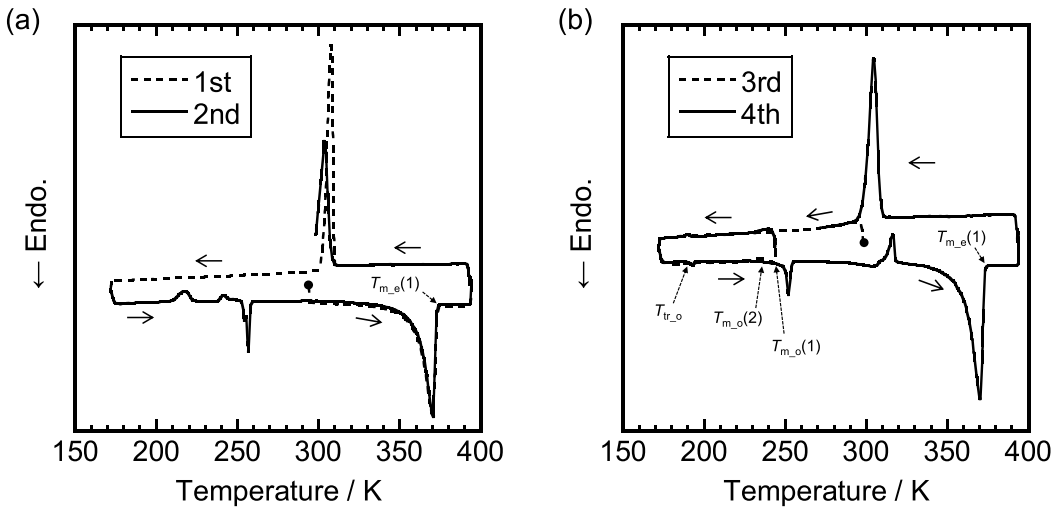

Figure S13 DSC curves for K[FSA]–[C_3C_1pyrr][FSA] (x(K[FSA]) = 0.90). Scan rate: 2 K min^{-1}. Holding temperature and time before 4th cycle: 243 K and 60 min.

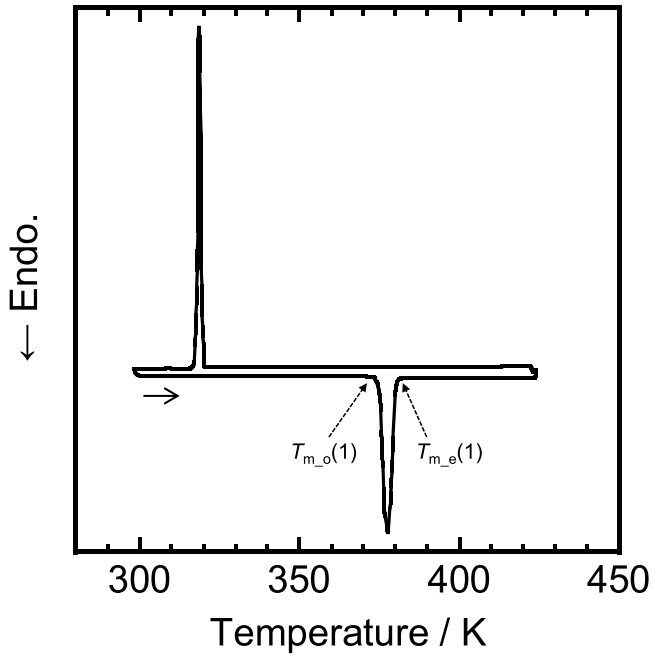

Figure S14 A DSC curve for K[FSA]. Scan rate: 2 K min^{-1}.

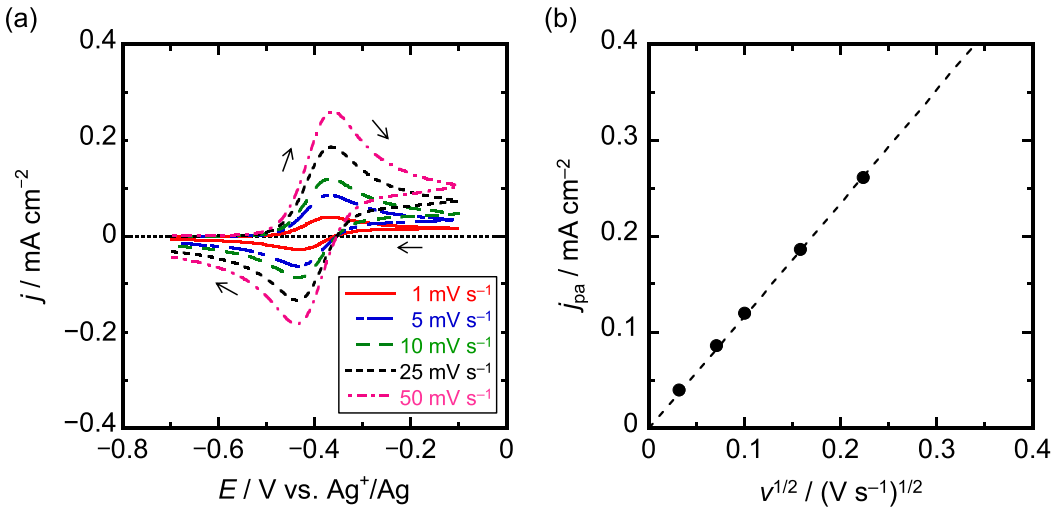

Figure S15 (a) Cyclic voltammograms of a platinum disk in K[FSA]–[C_3C_1pyrr][FSA] ionic liquid (x(K[FSA]) = 0.20) containing 10 mmol dm^{-3} ferrocene. Scan rates: 1–50 mV s^{-1}. Temperature: 298 K. (b) Correlation plots of current densities and the square root of scan rates.

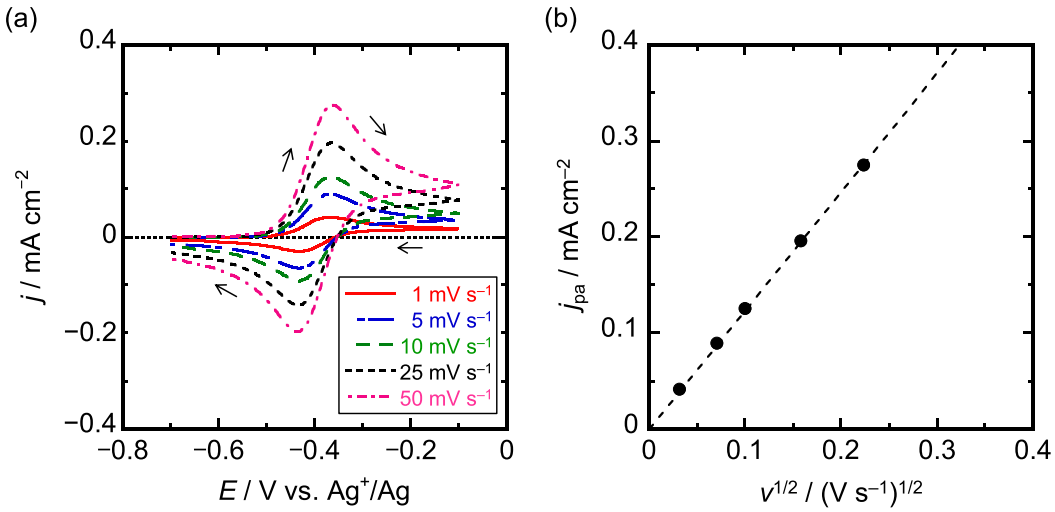

Figure S16 (a) Cyclic voltammograms of a platinum disk in Na[FSA]–[C_3C_1pyrr][FSA] ionic liquid (x(Na[FSA]) = 0.20) containing 10 mmol dm^{-3} ferrocene. Scan rates: 1–50 mV s^{-1}. Temperature: 298 K. (b) Correlation plots of current densities and the square root of scan rates.

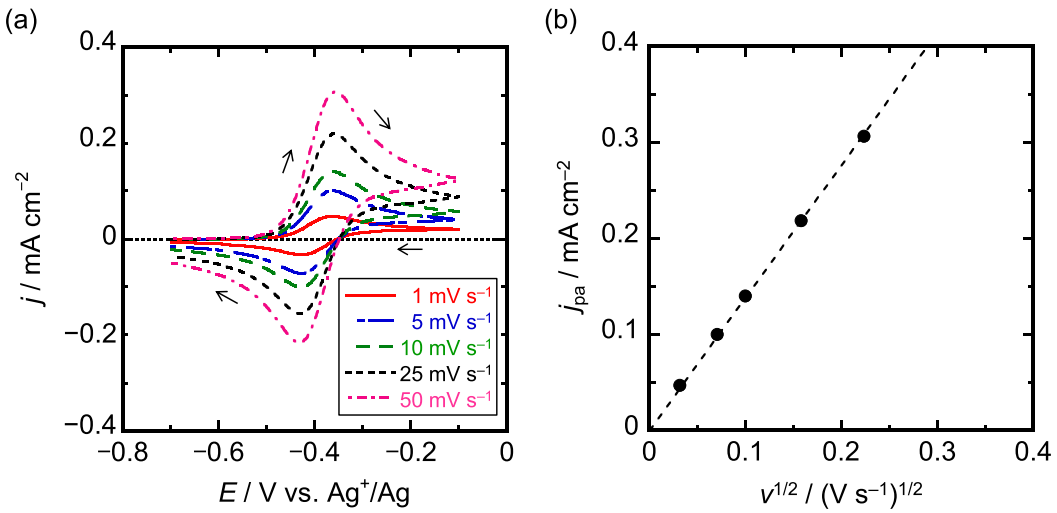

Figure S17 (a) Cyclic voltammograms of a platinum disk in Li[FSA]–[C_3C_1pyrr][FSA] ionic liquid (x(Li[FSA]) = 0.20) containing 10 mmol dm^{-3} ferrocene. Scan rates: 1–50 mV s^{-1}. Temperature: 298 K. (b) Correlation plots of current densities and the square root of scan rates.

As shown in **Figures S15**–**S17**, the reaction of ferrocenium cation/ferrocene couple (Fc^+/Fc) is considered to be reversible. Assuming the diffusion coefficients of the oxidant and the reductant are almost same, the formal potential of the reaction can be calculated as follows;[a]

$$E^{\circ\prime} \approx \frac{E_{pa} + E_{pc}}{2} \qquad \text{(A-1)}$$

where $E^{\circ\prime}$ is the formal potential, E_{pa} is the peak potential during the positive potential sweep, and E_{pc} is the peak potential during the negative potential sweep. The diffusion coefficients of ferrocene can be calculated from the correlation plots between current densities and the square root of scan rates. For the reversible reaction, these plots are fitted by the following equation;[a]

$$j_{pa} = 0.4463 \times \left(\frac{F^3}{RT} \right)^{1/2} n^{3/2} D_R{}^{1/2} C_R v^{1/2} \qquad \text{(A-2)}$$

where j_{pa} is the current density (in A cm^{-2}), F is the Faraday constant (in C mol^{-1}), R is the gas constant (in J mol^{-1} K^{-1}), T is temperature (in K), n is the stoichiometric number of electrons involved in an electrode reaction, D_R is the diffusion coefficient of the reductant (in cm^2 s^{-1}), C_R is the concentration of the reductant (in mol cm^{-3}), and v is the scan rate (in V s^{-1}). The obtained diffusion coefficients of ferrocene are 1.9×10^{-7} cm^2 s^{-1}, 2.1×10^{-7} cm^2 s^{-1}, and 2.6×10^{-7} cm^2 s^{-1} in K[FSA]–[C_3C_1pyrr][FSA], Na[FSA]–[C_3C_1pyrr][FSA], and Li[FSA]–[C_3C_1pyrr][FSA] ionic liquids, respectively. These values are close to other ionic liquids.[b,c]

(a) Bard, A. J.; Faulkner, L. R. *Electrochemical Methods: Fundamentals and Applications,* 2nd ed., John Wiley & Sons, NY, US, (2001).

(b) Fuller, J.; Carlin, R. T.; Osteryoung, R. A. The Room Temperature Ionic Liquid 1-Ethyl-3-methylimidazolium Tetrafluoroborate: Electrochemical Couples and Physical Properties. *J. Electrochem. Soc.* **1997**, *144*, 3881–3886.

(c) Yamagata, M.; Tachikawa, N.; Katayama, Y.; Miura, T. Electrochemical behavior of several iron complexes in hydrophobic room-temperature ionic liquids. *Electrochim. Acta* **2007**, *52*, 3317–3322.